

Article

Crystallization Kinetics: Relationship between Crystal Morphology and the Cooling Rate—Applications for Different Geological Materials

Namık Aysal ^{1,*}, Yiğit Kurt ², Hüseyin Öztürk ¹, Gulce Ogruc Ildiz ³, Mehmet Yesiltas ⁴, Davut Laçın ¹, Sinan Öngen ¹, Timur Nikitin ⁵ and Rui Fausto ^{3,5}

¹ Geological Engineering Department, Istanbul University-Cerrahpaşa, 34555 Istanbul, Turkey; ozturkh@iuc.edu.tr (H.Ö.); davut@iuc.edu.tr (D.L.); asinanongen@gmail.com (S.Ö.)

² Graduate Institute, Istanbul University, 34320 Istanbul, Turkey; yigitkurt34@gmail.com

³ Department of Physics, Faculty of Sciences and Letters, Istanbul Kultur University, 34197 Istanbul, Turkey; g.ogruc@iku.edu.tr (G.O.I.); rfausto@ci.uc.pt (R.F.)

⁴ Faculty of Aeronautics and Space Sciences, Kırklareli University, 39100 Kırklareli, Turkey; myesiltas@knights.ucf.edu

⁵ CQC-IMS—Department of Chemistry, University of Coimbra, P-3004-535 Coimbra, Portugal; timur.nikitin@uc.pt

* Correspondence: aysal@iuc.edu.tr

Abstract: Crystal morphology is controlled by several physicochemical parameters such as the temperature, pressure, cooling rate, nucleation, diffusion, volatile composition, and viscosity. The development of different crystal morphologies is observed as a function of the cooling rate in many different rock types (i.e., glassy volcanic rocks, and archeometallurgical slags). Crystallization is a two-stage kinetic process that begins with the formation of a nucleus and then continues with the accumulation of ions on it. The shapes of the crystals depend on the degree of undercooling (ΔT), and euhedral crystals, having characteristic forms that reflect their crystallographic internal structure, that grow just below their liquidus temperature. In this study, crystal morphologies in different minerals (e.g., quartz, sanidine, olivine, pyroxene, magnetite, etc.) that had developed in silicic volcanic rocks (spherulites) and slags from ancient mining were investigated and characterized using optical microscopy, X-ray diffraction, and Fourier-transform infrared (FTIR), Raman, and scanning electron microscope-energy dispersive X-ray fluorescence (SEM-EDX) spectroscopic techniques. Depending on the increase in the cooling rate, quartz, feldspar, olivine, pyroxene, and magnetite minerals were found to crystallize in subhedral, skeletal, dendritic, spherical, bow-tie and fibrous forms in glassy volcanic rocks and archeometallurgical slags.

Keywords: crystallization kinetics; undercooling; crystal morphology; archeometallurgical slags



Citation: Aysal, N.; Kurt, Y.; Öztürk, H.; Ildiz, G.O.; Yesiltas, M.; Laçın, D.; Öngen, S.; Nikitin, T.; Fausto, R. Crystallization Kinetics: Relationship between Crystal Morphology and the Cooling Rate—Applications for Different Geological Materials. *Crystals* **2023**, *13*, 1130. <https://doi.org/10.3390/cryst13071130>

Academic Editors: Chiara Castiglioni and Bernardo A. Nogueira

Received: 24 June 2023

Revised: 13 July 2023

Accepted: 16 July 2023

Published: 19 July 2023



Copyright: © 2023 by the authors. Licensee MDPI, Basel, Switzerland. This article is an open access article distributed under the terms and conditions of the Creative Commons Attribution (CC BY) license (<https://creativecommons.org/licenses/by/4.0/>).

1. Introduction

Crystal morphologies provide important information about the physicochemical conditions that control the crystallization processes of both natural (terrestrial or extraterrestrial) and synthetic materials; however, the different crystal morphologies in natural and synthetic materials are still not fully understood. Depending on the temperature and pressure, many parameters such as the cooling rate of the melts, nucleation, volatile components, and viscosity, directly affect the crystal morphology. Minerals have specific crystallographic forms as a reflection of their atomic internal structure; however, minerals can fully reflect these crystallographic forms only when they crystallize under ideal conditions. As a result of the change in the parameters controlling the crystallization process, the crystals may exhibit different morphologies, which reflect the new crystallization conditions. The textures observed in rocks are reflective of their formation conditions, which are determined by the degree of crystallization, crystal size, rate of crystallization, and crystal shape.

The development of different crystal textures as a function of the cooling rate can be observed in many rock types and inorganic polymers [1–12], both in natural conditions and in experimental studies, and the results of the crystallization of minerals from a melt can also be observed in slags obtained from archeometallurgical processes [13]. Since minerals may exhibit different crystal textures and morphologies [14], it is sometimes difficult to define and characterize newly formed crystal morphologies and mineral phases; thus, advanced analytical methods (e.g., XRD, and Raman, FTIR and SEM-EDX spectroscopies) are needed for the identification and characterization of these phases. In this study, a set of natural and artificial geological materials were characterized for the first time by different diffractometric and spectroscopic methods. As a result, major and minor mineralogical compositions, crystal morphologies and the formation conditions of spherulites in siliceous volcanic rocks and of ancient-mine slags have been described in detail.

2. Materials and Methods

2.1. Materials

Two different geological materials (spherulites and slags) were investigated in this work. The spherulites were collected from a perlite level in the rhyolitic lava succession south of Işikeli village (Lat.: 40°9′38.96″ N—Long.: 27°17′58.52″ E; Biga-Çanakkale-Turkey; [15]). The slag samples were collected from the ancient copper mine of Dereköy (NW Turkey). These slags were obtained upon the smelting of copper ores belonging to the Bahtiyar Hill skarn mineralization with primitive methods, in the temperature range of 1000–1100 °C, in the ancient A.D. 72–219 period [16]. Since a standard method was not used in the ore preparation and melting, the slag samples did not show a homogeneous composition. Prefixes prepared from relatively coarse crystalline parts close to their outer walls were used in this study.

2.2. Methods

Thin sections were prepared to describe the mineralogical composition and textural properties of the spherulites and slag samples. Transparent minerals in the prepared sections were examined using a Leitz Ortoplan polarizing microscope (Ernst Leitz, Wetzlar, Germany), and a reflective microscope was used to visualize the opaque minerals. The mineral phases and textural features were visualized using Leica image analysis systems attached to the microscope.

The X-ray diffraction (XRD) analyses were carried out at the XRD laboratory of the Istanbul University-Cerrahpaşa, Department of Geological Engineering. This laboratory is equipped with a Philips PW-1730 X-ray diffractometer system (Netherlands). The diffraction data were acquired by exposing powder samples to Cu-K α X-ray radiation, which has a characteristic wavelength (λ) of 1.5418 Å. The X-rays were generated from a Cu anode supplied with a voltage of 40 kV and a current of 20 mA. A goniometer speed of $2\theta = 1^\circ/\text{min}$ was used during the analyses. The data were collected over a range of 10–65° 2θ values. The analysis of the X-ray patterns (i.e., phase identification) was carried out by using the Philips High Score Plus software in conjunction with the Joint Committee on Powder Diffraction Standards (JCPDS) database.

The BSE imaging and SEM-EDX analyses of the spherulite and slag samples were performed by using a Hitachi SU4000 SEM device and an attached Oxford XACT EDX spectrometer, while the XRF analyses were performed by using a Rigaku Supermini 200 XRF spectrometer available at the TETRA Technological Systems (Istanbul, Turkey) laboratories. The acceleration voltage was fixed at 15 kV, and the beam current was adjusted to be different according to the mineral dimensions. SRM NIST 610 glass was used as the control standard to ensure precision of the method during the EDS analyses, with the analytical uncertainty of the measurement after every ten points for major oxides being less than 0.1%.

Raman measurements were performed on different pieces cut from the same sample, in two different laboratories. One set of Raman spectroscopic data was collected at the University of Coimbra using a Horiba LabRAM Evolution confocal micro-Raman system

(HORIBA France SAS), equipped with a $\times 50$ long-range objective, with the excitation at 532 nm (~ 5 mW on the sample; ~ 1 μm spot size). The calibration of the system was performed using as the reference the silicon crystal Raman peak at 520.5 cm^{-1} . To produce the Raman maps, two-dimensional spectral arrays of the Raman spectra were collected from a rectangular region ($170 \times 300\ \mu\text{m}$) with vertical and horizontal steps of $5\ \mu\text{m}$, a 5 s exposure time and 5 accumulations at each point. The Raman maps for each group of three minerals (see details below) were produced in the LabSpec 6.6.1.14 software by integrating their characteristic Raman bands. The following image parameters were used to construct the Raman maps: (i) Auto Intensity Scale: “enabled”; (ii) Display Mode: “overlay and normalize”; (iii) Color Mixing: “maximum”; and (iv) Smoothing: “smoothed”. A classical least squares (CLS) fitting procedure provided by the LabSpec 6.6.1.14 software was also applied to the two-dimensional spectral arrays of the Raman spectra using several sets, with each containing three reference component spectra (loadings) of minerals taken from the RRUFF database [17]. The following options were used for the CLS fitting procedure: (1) “normalize loadings”, which normalize the loadings by intensity; and (2) Constraints: “positive”, which keeps only positive scores during the fitting process. The resulting images were produced with the following parameters: (i) Auto Intensity Scale: “enabled”; (ii) Display Mode: “overlay and normalize”; (iii) Color Mixing: “mixed”; and (iv) Smoothing: “no smoothed”.

The other Raman spectroscopy datasets were collected at the Gazi University, using a confocal Raman imaging micro spectroscopy system, namely, the WiTec alpha300R (Ulm, Germany). The system consists of a 600 g/mm grating, a 532 nm Nd:YAG laser, and a $50\times$ objective (NA = 0.8). The spectrograph was calibrated using a silicon wafer substrate prior to the measurements. Individual Raman spectra were collected between $0\text{--}4000\text{ cm}^{-1}$, using 60 accumulations with a 1 s integration time. Hyperspectral Raman maps were collected with a $0.5\ \mu\text{m}$ pixel size with a $0.1\text{--}0.3$ s integration time. The laser power was $\sim 1\text{--}3$ mW on the sample surface throughout the data acquisition. Intensity distribution maps of the individual chemical components were generated by integrating the signal between the spectral endpoints of the Raman peaks using the WITec Project software package.

The infrared attenuated total reflectance (ATR) infrared spectra of the powdered spherulite and slag samples were recorded using a Jasco 6700 FTIR spectrometer (Jasco, Japan) located in the Fatih Sultan Mehmet Vakıf University (FSMVU—KURAM). The spectra were recorded in the $4000\text{--}400\text{ cm}^{-1}$ range, with a DLaTGS detector, by using an ATR module with a 4 cm^{-1} resolution. Each spectrum was obtained by averaging 32 scans. The Spectra Manager controlling software package was used, and the spectrum of air was used as the background.

3. Results

3.1. Mineralogical and Textural Characterization

3.1.1. Spherulite

Spherulites and axiolites up to 12 cm in size developed along vertical cooling cracks within the brown-green colored perlite levels [18] (Figure 1a,b). Spherulites are macro and/or micro spherical formations that are formed by the radial arrangement of acicular, fibrous, and needle-like feldspars and quartz crystals (i.e., cryptocrystalline intergrowths) during eutectic crystallization in glassy volcanic rocks. Spherulites are mostly secondary formations in the devitrification of glassy ground mass in silicic volcanic rocks and are not phenocrystals. Spherulites typically consist of quartz (and/or tridymite, and cristobalite) and feldspar (orthoclase, and sanidine) with minor amounts of Fe–Ti oxides and volcanic glass between the fibers. Spherulites also contain minor minerals such as magnetite, pyrite and rutile. Mineral fibers can be arranged in spherical (Figure 1c), bow-tie (Figure 1d), fan (Figure 1e), plumose or axiolic shapes [19] (Figure 1e,f). Spherulites are characterized by a radial arrangement of quartz and feldspar minerals, situated beneath a thin, green-colored crust on the outer surface. At the center, a crypto-crystalline core can be found (Figure 1c).

Among the spherulite layers are axiolites with the appearance of elongated spherulites. Under the polarizing microscope, in the crossed-polarized light position, the dark cross-shaped extinction was typical, and this cross remained constant when the table was rotated (Figure 1c,d). Petrographic observations showed that the small spherulites in the perlite glass were cut by the axiolites in the later stage (Figure 1f). Based on XRD analyses, the mineralogical composition of the spherulites was found to consist mainly of Na-sanidine and, to a lesser extent, cristobalite minerals (Figure 2), while the infrared spectroscopy data showed that the spherulite spectrum was very similar to that of sanidine, thus reinforcing the conclusions extracted from the XRD measurements. The infrared ATR spectrum of the spherulite contained two main bands at 1085 and 1000 cm^{-1} . The latter was the most prominent band and was also present in the spectra of the sanidine (as well as in that of the microcline) (Figure 3). Other bands were observed at 786, 715, 637, 583, 546, and 465 cm^{-1} , all of which were also present in the sanidine reference spectrum (with the exception of the band at 465 cm^{-1}).



Figure 1. (a,b) Spherulites and axiolites in perlite glass; (c) spherulitic; (d) bow-tie; (e) fan or plumose; and (f) axioitic morphologies formed by acicular cristobalite and Na-Sanidine crystals in glassy groundmass.

The Raman spectra used to build the maps shown in Figure 4 were first analyzed for identification of the minerals present in the sample, by a comparison of the individual spectra with the reference Raman spectra of minerals of the RRUFF spectral database [17]. In consonance with the XRD and petrographic analyses, Na-sanidine and cristobalite were identified as the major constituents of the studied spherulite; however, several other minerals were also identified as minor components. Figure 4a–d displays an optical microscope image of a selected representative region of the spherulite sample, as well as the same optical image superimposed with the corresponding Raman maps from the CLS analysis. The Raman data show the distribution of the two major mineral components (Na-sanidine and cristobalite) in the studied region, as well as of some of the minerals present in the sample as minor components. Each panel with Raman data shows the distribution of a specific minor component (in red color) over the background defined by the two major components (sanidine in green color and cristobalite in blue), in particular, pyrite (Figure 4b),

barite (Figure 4c), and magnetite (Figure 4d). The spectral regions, used to identify each of the components plotted in the Raman maps, are indicated in the corresponding figure. Rutile, calcite and anatase were also identified in the Raman experiments, with the last two minerals being less abundant in the sample than the remaining minor constituents identified. Pyrite was mostly distributed in the sanidine-rich areas, and barite, rutile and magnetite were predominantly distributed in the cristobalite-rich areas.

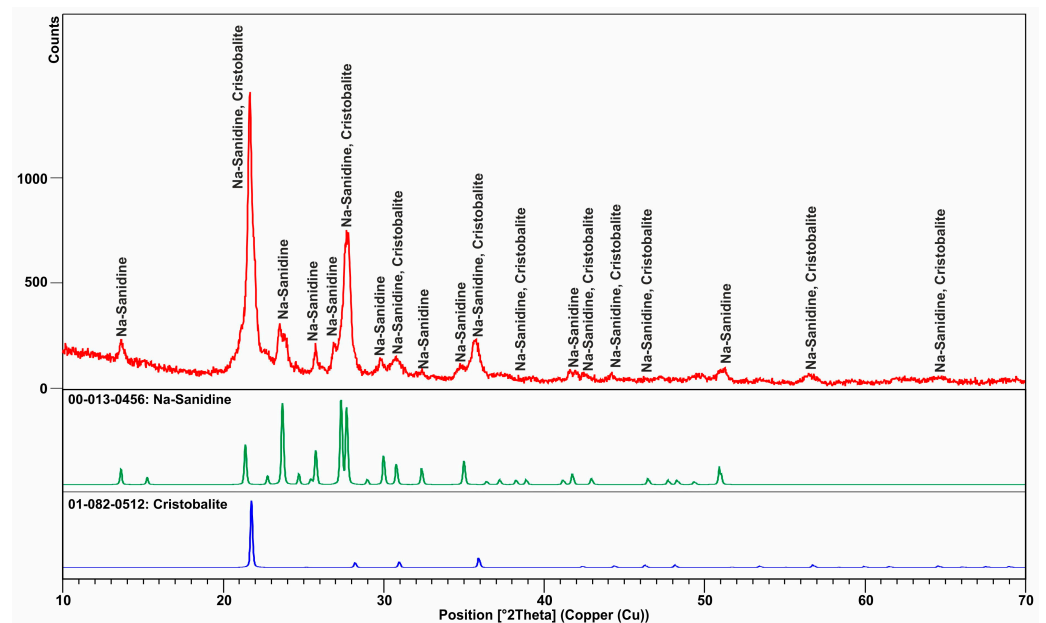


Figure 2. XRD pattern and described mineral composition of the spherulite.

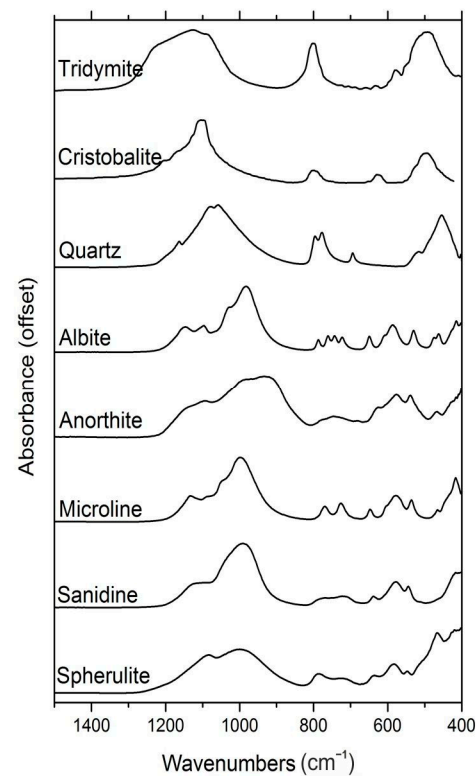


Figure 3. FTIR spectra of spherulite and reference feldspars for comparison. Spherulite spectrum is best represented by sanidine. The reference spectra are from RRUFF [17].

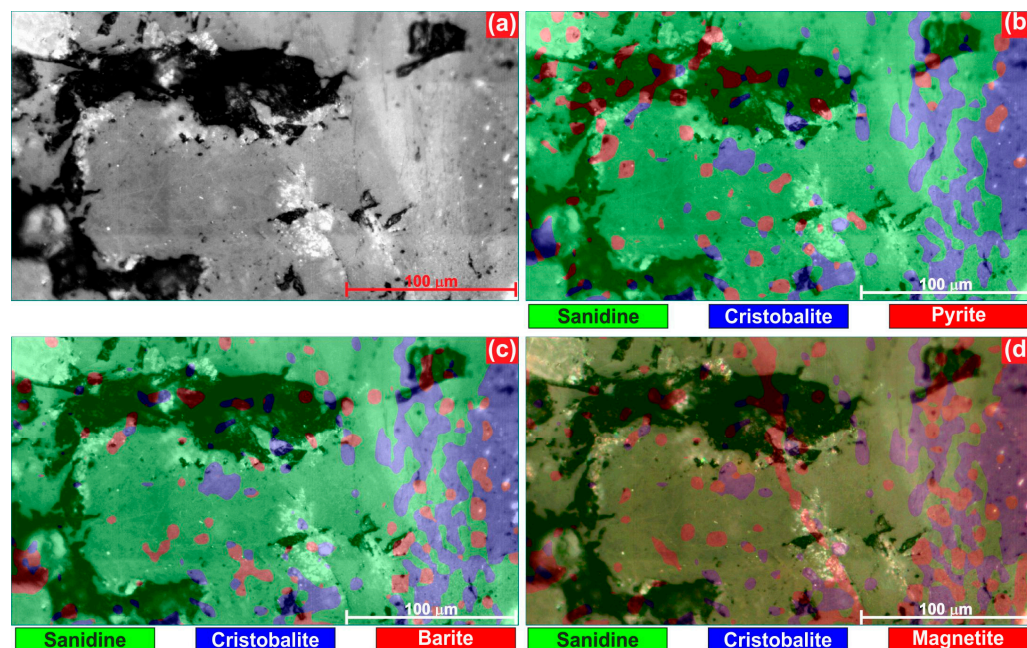


Figure 4. Optical image of a selected region of the spherulite sample ($\sim 170 \times 300 \mu\text{m}$) (a), and Raman maps (collected at University of Coimbra), CLS results with reference spectra of sanidine, cristobalite, pyrite, barite and magnetite taken from the RRUFF database (b–d) superimposed on the same optical image.

The backscattered electron (BSE) imaging and EDX elemental mapping show that the spherulite exhibited a chemically-heterogeneous structure (Figure 5a,b). The elemental distribution in different regions (A-2 to A-4) of the spherulite typically reflected a rhyolite composition (Table 1). The EDX analysis of the spherulite resulted in amounts of SiO_2 ranging from 77.02 to 78.61 wt.%, Al_2O_3 from 12.17 to 13.01 wt.%, FeO from 0.6 to 0.78 wt.%, CaO from 0.94 to 1.01 wt.%, Na_2O from 3.9 to 5.16 wt.%, and K_2O from 2.68 to 4.35 wt.%; however, in point measurements, some points typically reflected a composition of Na-sanidine, while other points reflected mixtures of cristobalite—Na-sanidine with high SiO_2 contents. These points (A-5 to A-9) had SiO_2 contents ranging from 66.29 to 89.58 wt.%, Al_2O_3 from 6.07 to 12.52 wt.%, FeO from 0.19 to 5.62 wt.%, CaO from 0.27 to 2.01 wt.%, Na_2O from 1.52 to 4.08 wt.%, and K_2O from 1.96 to 6.23 wt.%.

Table 1. EDX and XRF (* Whole-rock) results (wt.%) for the spherulite and slag samples.

	SiO_2	TiO_2	Al_2O_3	FeO	MnO	MgO	CaO	Na_2O	K_2O	P_2O_5	BaO	SO_3	Cu	Total
A-1	77.96		12.64	0.6			0.96	5.16	2.68					100
A-2	78.54		12.74				1.01	4.94	2.77					100
A-3	78.61		12.17	0.6			0.95	4.82	2.85					100
A-4	77.02		13.01	0.78			0.94	3.9	4.35					100
A-5	89.58		6.07	0.2			0.27	1.52	2.36					100
A-6	66.94	1.3	12.52	5.38			0.47	2.35	6.23		3.05	1.76		100
A-7	70.04		11.94	5.62	0.74	3.13	2.01	2.79	3.29		0.44			100
A-8	66.29	1.3	11.77	0.69			0.98	4.08	1.96		8.04	4.89		100
A-9	78.49		11.75	0.19	0.53		0.5	2.72	5.4		0.42			100
S-1A	42.1	0.27	7.7	27.62	0.57	3.35	16.17		1.25	0.38			0.59	100
S-2A	42.15	0.25	7.6	28.72	0.88	2.9	15.65		1.3	0.34			0.21	100
S-1P	36.46		2.23	45.13	0.95	9.39	5.49		0.35					100
S-2P	35.99		2.44	45.76	1.01	8.41	5.94		0.45					100

Table 1. Cont.

	SiO ₂	TiO ₂	Al ₂ O ₃	FeO	MnO	MgO	CaO	Na ₂ O	K ₂ O	P ₂ O ₅	BaO	SO ₃	Cu	Total
S-3P	45.2		8.33	23.53		2.39	19.89		0.66					100
S-3A	26.6	0.15	2.89	50.7	0.47	1.84	14.8		0.32	0.19		0.2	1.84	100
S-4A	26.78		3.95	48.12	0.54	2.28	17.04		0.34				0.95	100
S-4P	4.49	0.31	3.98	87.38	0.28	1.17	2						0.39	100
S-5P	31.11		2.13	37.06	0.71	4.18	24.81							100
S-6P	37.5	0.16	6.3	31.92	0.36	0.99	22.34		0.11				0.32	100
S-7P	5.36	0.23	4.25	86.71		0.77	2.68							100
S-8P	37.07		11.03	26.26	0.38	0.44	16.35	0.83	3.43	1.91			2.3	100
DR-1 *	38.6	0.26	7.48	32.3	0.62	3.12	14.70	0.58	1.16	0.32		0.29	0.50	99.93
DR-12 *	29.5	0.09	3.01	46.1	0.49	2.40	15.30	0.27	0.28	0.22		0.18	2.10	99.92

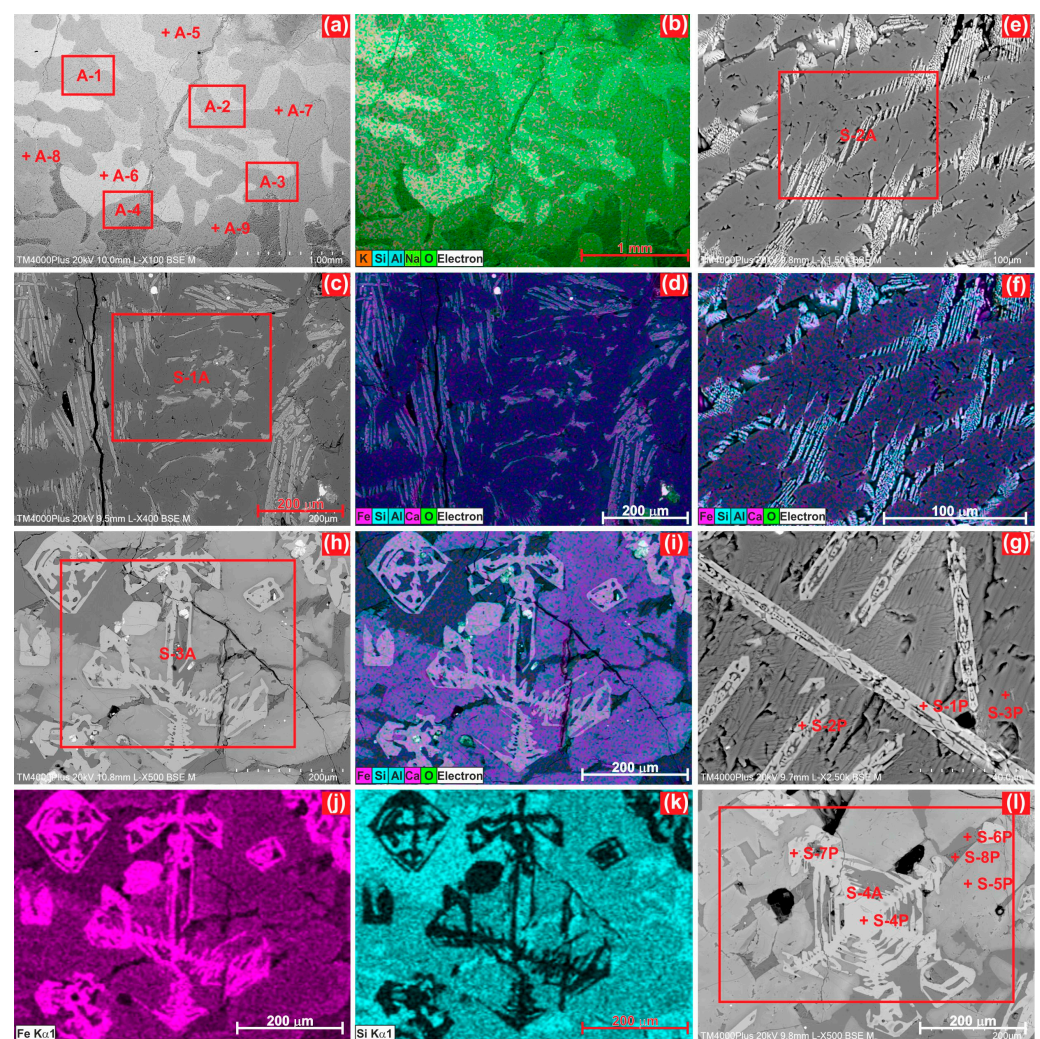


Figure 5. BSE images and SEM-EDX elemental mapping of the spherulite (a,b) and slag samples (c–i).

3.1.2. Slags

The slag samples (DR-1 to DR-12) taken from the ancient copper mine of Dereköy had oval edges and a distinctive flowing structure. The diameter of the slags was at least 22 cm; they were dark gray–blackish in color and their oxidized surfaces were brown–reddish. They contained gas bubbles ranging from micron to cm in size, and also pieces of charcoal, molten copper prills (Figure 6a,b), and granite fragments that had fallen into the furnace. These granite pieces were covered with dark gray–brown malachite; however, they generally consisted of a glassy ground mass. The relative mineral textures and compositions

of the slags changed from the center to the outer walls. The pyrometallurgical phases were represented by fayalite (Fe_2SiO_4), and kirschsteinite (CaFeSiO_4), and/or monticellite (CaMgSiO_4), hedenbergite ($\text{CaFeSi}_2\text{O}_6$), diopside ($\text{CaMgSi}_2\text{O}_6$), magnetite (Fe_3O_4), and Cu-rich metal sulfides and droplets in the glassy matrix. Dendritic crystals and a partially glassy matrix formed the internal structures of the slags (Figure 6c). Dendritic, elongated, skeletal and coarse-grained olivine group minerals (fayalite—kirschsteinite—monticellite solid solutions) were quite prominent under the polarizing microscope. A glassy matrix, greenish hedenbergite, and opaque minerals (i.e., magnetite, hematite and/or wüstite, copper droplets) were observed among the colorless or pale green–yellow colored olivine crystals (Figure 6d,e,g–i). The glassy matrix was generally ubiquitous, especially in the rapidly cooled slags. It was observed that the crust, the interior of the gas cavities and the fractured surfaces of the examined slags were glassy. Conversely, the interior of the slags was rich in crystals and a clear glass pattern was not observed in the XRD analysis (Figure 7); therefore, the slags were crystalline slags. The olivine group minerals had strong, third-order interference colors under a crossed polarized light. The green-colored pyroxenes (i.e., hedenbergite and/or diopside) had grown on the margins of dendritic olivine crystals as zones surrounding the olivine's. They were also observed as single hedenbergite crystals (Figure 6g) under the plain polarized light. Irregular magnetite needles forming the metallic mineral phases between the olivine crystals were easily distinguished under the reflected polarizing microscope (Figure 6f). Plagioclase, pyroxene (hedenbergite, and diopside), and skeletal magnetite minerals were determined to be present in some slag samples (Figure 6j,k). Skeletal magnetite minerals were also identified under the reflected polarizing microscope (Figure 6l).

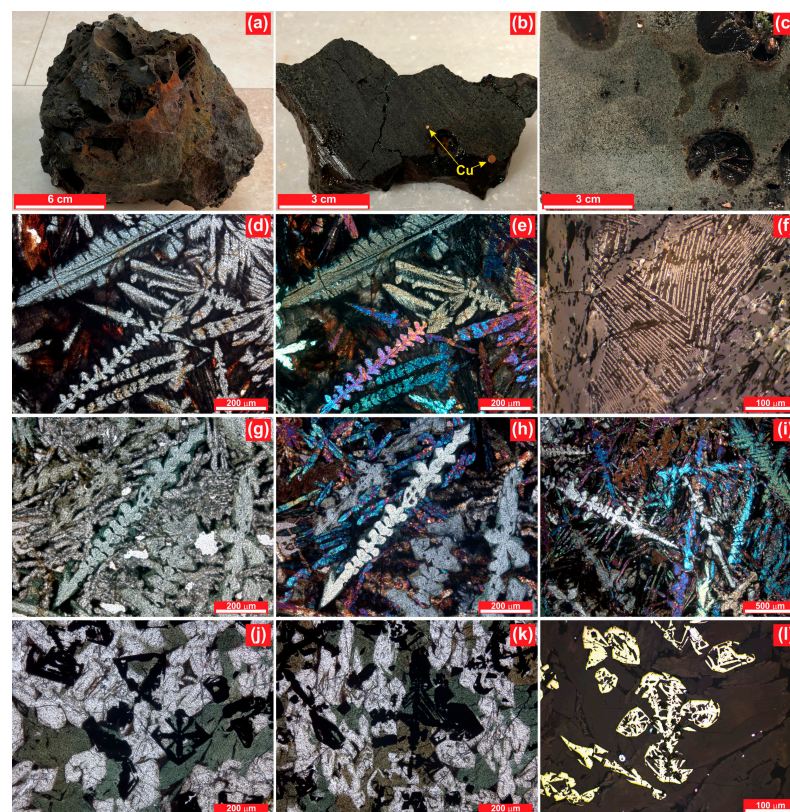


Figure 6. Macro examples of slags: (a) tubular voids from charcoal, (b) copper prills, and (c) partially-glassy matrix containing dendritic crystals. Polarizing microscope images of slags containing skeletal olivine (colorless) and hedenbergite (pale green-colored) minerals (d,g): plane polarized light (PPL); and (e,h,i): crossed-polarized light (CPL)). Reflective (f,l) and polarized microscope (j,k) images of irregular magnetite needles and skeletal magnetite crystals.

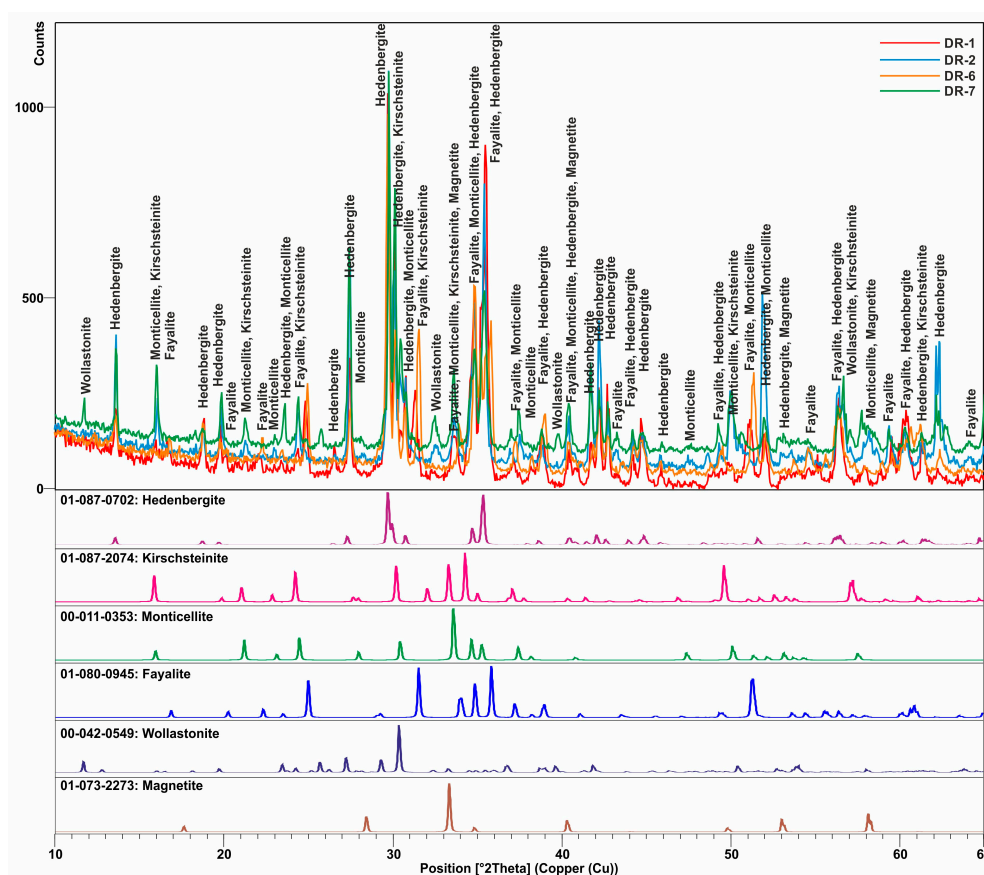


Figure 7. Representative XRD patterns of slag samples.

Olivine, pyroxene, and magnetite minerals were commonly identified in the studied slag samples using an X-ray powder diffraction analysis, while hematite, wollastonite, garnet (andradite), plagioclase, and quartz minerals were detected in minor amounts (Figure 7). After the XRD analysis, three different slag samples (i.e., DR-1, DR-7, and DR-12) were selected for the determination and mapping of the mineralogical phases by Raman spectroscopy. Skeletal olivine (fayalite) crystals were clearly identified in the DR-1 sample. It is seen that the crystals were surrounded by a glassy matrix (Figure 8a–c). In addition, detailed Raman imaging of hooper type fayalite crystals (Figure 9a,b) revealed that the glassy part around the fayalite minerals was of a hedenbergite composition and that less chalcopyrite minerals were present. The Raman data allowed us to identify kirschsteinite and hedenbergite as major constituents of the DR-7 sample, as shown in Figure 8c–e. Wollastonite and carbon inclusions were also identified as minor constituents, appearing to be present predominantly in locations in the sample close to the hedenbergite (see Figure 8c–e). In addition, in the DR-12 sample, skeletal magnetite crystals and surrounding pyroxenes (hedenbergite-diopside) were clearly identified (Figures 8d–f and 9f,g).

The infrared spectra of the studied slags are shown in Figure 10 (top panel). All the slags presented almost identical infrared spectra, with the exception of DR-12. The 1200–800 cm^{-1} region exhibited bands at 1056, 955, and 864 cm^{-1} . The spectral differences observed for DR-12 when compared to the other slags reflected the constituting difference of the sample. The spectrum of DR-12 resembled an olivine spectrum, best represented by the fayalite spectrum. The 800–400 cm^{-1} spectral regions presented several relatively weaker bands. These bands were observed at 667, 627, 501, and 456 cm^{-1} . Based on their infrared spectra, the slags resembled kirschsteinite, diopside, and hedenbergite.

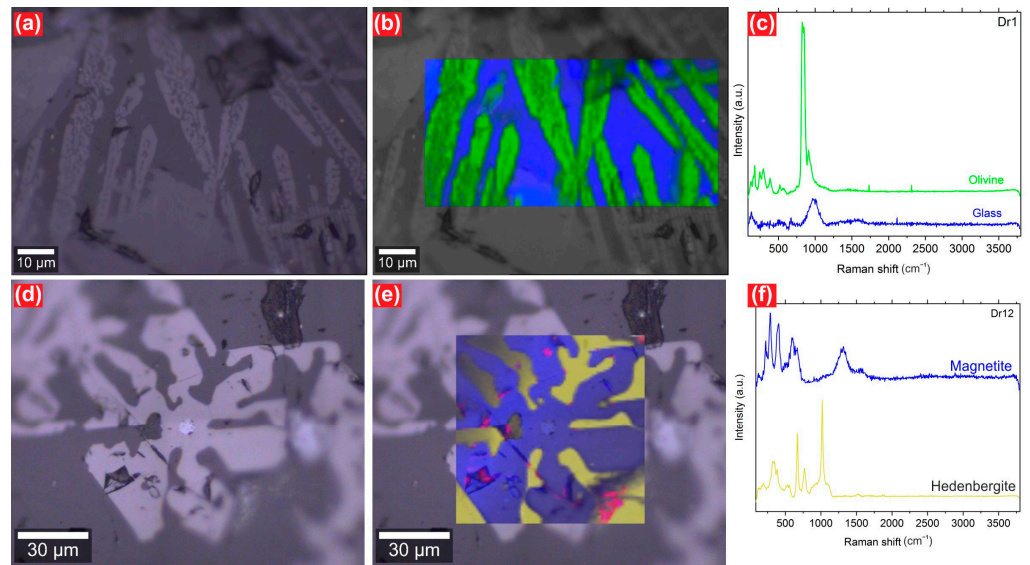


Figure 8. Optical image of a selected region on the DR-1 (a–c), and DR-12 (d–f) samples, Raman maps (collected at Gazi University) of CLS results with reference spectra of olivine, hedenbergite, and magnetite taken from the RRUFF database superimposed on the corresponding optical images of DR-1 (b), and DR-12 (e) samples, as well as typical Raman spectra for DR-1 (c) and DR-12 (f) samples.

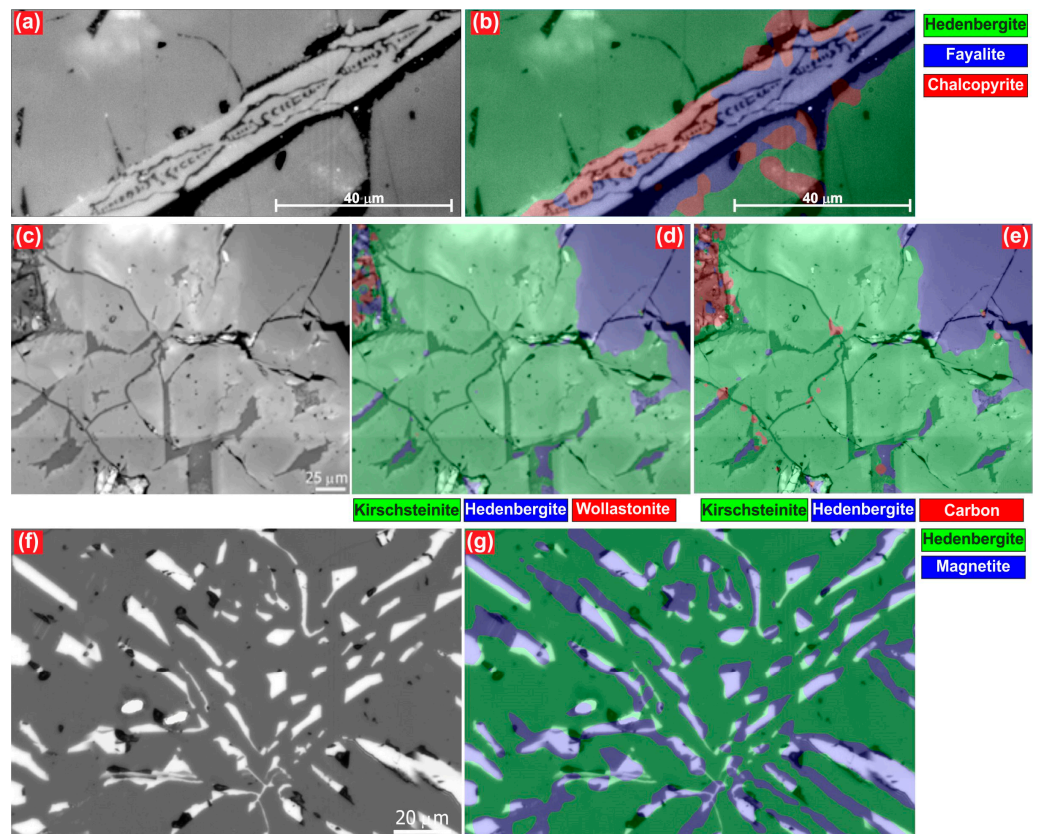


Figure 9. Optical images of selected regions of the DR-1 (a), DR-7 (c), and DR-12 (f) samples, as well as Raman maps (collected at University of Coimbra) of CLS results with reference spectra of fayalite, kirschsteinite, hedenbergite, diopside, wollastonite, carbon, and magnetite taken from the RRUFF database superimposed on the corresponding optical image of the samples DR-1 (b), DR-7 (d,e), and DR-12 (g).

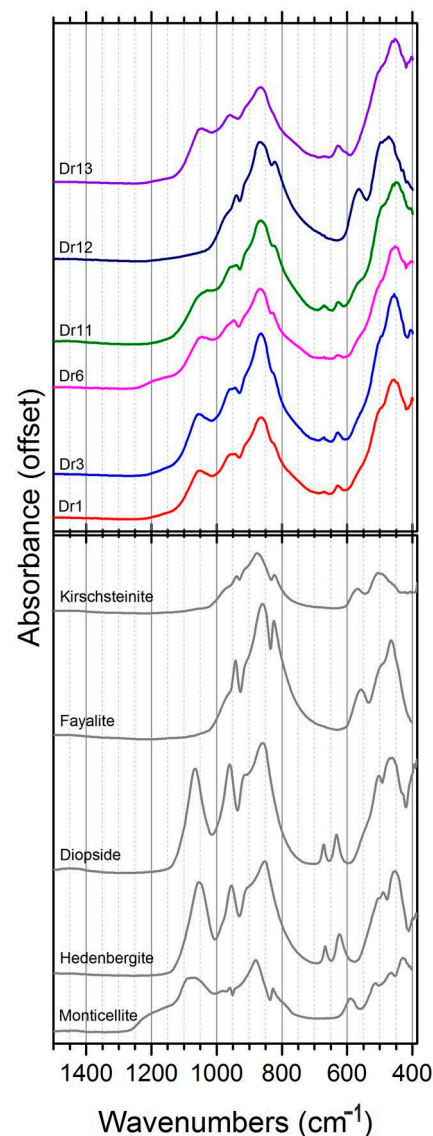


Figure 10. FTIR spectra of slags (**top** panel) and mineral standards (**bottom** panel, from RRUFF [17]) for comparison.

The BSE images of the slag samples further confirmed the common mineralogical composition established from the petrographic observations, and the XRD and Raman analyses (Table 1; Figure 5c–l). The EDX analyses show that olivine minerals were mostly in the composition of kirschsteinite, and to a lesser extent monticellite and fayalite. The EDX analyses for the selected areas on the slag samples (i.e., S-1A to S-4A, Table 1; Figure 5) revealed SiO₂ contents ranging from 26.6 to 42.15 wt.%, TiO₂ from 0.15 to 0.25 wt.%, Al₂O₃ from 2.89 to 7.7 wt.%, FeO from 27.62 to 50.7 wt.%, MnO from 0.47 to 0.88 wt.%, MgO from 1.84 to 3.35 wt.%, CaO from 14.8 to 17.04 wt.%, K₂O from 0.32 to 1.3 wt.%, and P₂O₅ from 0.19 to 0.38 wt.%. The olivine minerals (i.e., S-1P and S-2P, Table 1; Figure 8g) had SiO₂ contents ranging from 35.99 to 36.46 wt.%, Al₂O₃ from 2.23 to 2.44 wt.%, FeO from 45.13 to 45.76 wt.%, MnO from 0.95 to 1.01 wt.%, MgO from 8.41 to 9.39 wt.%, CaO from 5.49 to 5.94 wt.%, and K₂O from 0.35 to 0.45 wt.%, and typically reflected a fayalite—kirschsteinite—monticellite solid solution chemistry. The pyroxenes (i.e., S-3P, S-5P, S-6P and S-8P, Table 1; Figure 5g–l) had SiO₂ contents ranging from 31.11 to 45.2 wt.%, Al₂O₃ from 2.13 to 11.03 wt.%, FeO from 23.53 to 37.06 wt.%, MnO from 0.36 to 0.71 wt.%, MgO from 0.44 to 4.18 wt.%, CaO from 16.35 to 24.81 wt.%, and K₂O from 0.11 to 3.43 wt.%, and typically reflected a hedenbergite—diopside solid solution chemistry. The skeletal

magnetites (i.e., S-4P, and S-7P, Table 1; Figure 5h–l) had SiO₂ contents ranging from 4.49 to 5.36 wt.%, TiO₂ contents ranging from 0.23 to 0.31 wt.%, Al₂O₃ from 3.98 to 4.25 wt.%, FeO from 86.71 to 87.38 wt.%, MgO from 0.77 to 1.17 wt.%, and CaO from 2 to 2.68 wt.%.

Whole-rock major oxide measurements made with XRF for the DR-1 and DR-12 slag samples (Table 1), yielded SiO₂ contents ranging from 29.5 to 38.6 wt.%, TiO₂ from 0.09 to 0.26 wt.%, Al₂O₃ from 3.01 to 7.48 wt.%, FeO from 32.30 to 46.10 wt.%, MnO from 0.49 to 0.62 wt.%, MgO from 2.40 to 3.12 wt.%, CaO from 14.70 to 15.30 wt.%, Na₂O from 0.27 to 0.58 wt.%, K₂O from 0.28 to 1.16 wt.%, and P₂O₅ from 0.22 to 0.32 wt.%.

4. Discussion

4.1. Nucleation Rate and Crystal Growth

There is a close relationship between the nucleation, crystal growth and texture depending on the thermodynamic equilibrium conditions [19]. Brandeis et al. (1984) [20] classified nucleation resulting from random thermal fluctuations in a liquid as a homogeneous nucleation. If the presence of another phase facilitated the process, they also classified it as heterogeneous nucleation. Nucleation generally develops heterogeneously on the pre-existing grains in a melt. The nucleus is formed by the juxtaposition of atoms or ions of a solid material with a regular lattice structure. Most of the nuclei will be re-melted before they can turn into large crystals because in the first stages of a regular structure, the surface area is much larger than the volume; that is, atoms with weak connections are located on the outer surface of a crystal and the structure can be disrupted [18]. Rapidly cooling rhyolitic melts form glassy volcanic rocks (obsidian and/or perlite), and if cooling occurs more slowly, a favorable environment for the nucleation and growth of crystal spherulites develop in hot glass [21]. Spherulites are formed due to heterogeneous nucleation or the devitrification of glass in undercooled (or supercooled) rhyolitic melts. Some studies have suggested that spherulites probably begin to form by heterogeneous nucleation on sub-microscopic seed crystals, bubbles, or fractures in a very undercooled (>150–200 °C) and highly viscous melt [22–26].

According to Watkins et al. [25], the occurrence of spherulites almost exclusively in glass requires conditions with a relatively fast rate of crystal growth as well as a low nucleation rate. They further suggested that their spherical shape may be due to the isotropic physical properties of the parent melt or glass, indicating the absence of any preferred growth direction or the non-crystallographic branching of mineral fibers [25]. Rosseeva et al. [26] suggested that the “non-crystalline branching” model is the driving force for spherulites formation and that this process begins with the formation of inhomogeneities in the growing crystal that induces a long-range stress field [26]. They argued that stress relaxation occurs through the nucleation, multiplication, and motion of dislocations to reduce elastic energy; thus, the formation of regular dislocation assemblages and other primary sub-individual crystals takes place at an early stage of branching, which may be somewhat misdirected with respect to the primary crystal matrix [26]. Individuals are isolated and grow independently in the next step. Additionally, the formation of individuals induces additional stress in the growing crystal and initiates the multiplication of individuals [27]. Rosseeva et al. [26] described further crystal branching as an autocatalytic process. According to them, if the branching is strong enough, a spherulite can wait for its formation and geometric selection processes play an important role at this stage. Finally, they emphasized that the process of formation of individuals in a crystal matrix is a stochastic phenomenon, and their growth is independently controlled only by external conditions (e.g., supersaturation, additives, temperature, etc.). Like nucleation, the rate of crystal growth also depends on the ΔT in the magma system. While increasing the ΔT is effective in crystal growth, ion mobility is delayed by a decreasing temperature and increasing viscosity. Three types are distinguished in crystal growth: growth as a result of chemical reaction at the liquid–solid boundary (euhedral crystals), diffusion-controlled growth (skeletal crystals), and growth by diffuse heat control (vigorous growth, that is observed in the direction of heat loss: dendrite, snow crystal, plumose, and bow-tie shaped

crystals) [18]. Experimental studies show that different crystal morphologies develop depending on the cooling rate (ΔT) and time (Δt) [28]. According to experimental studies [28], when a melt cools very slowly ($\Delta T < 10^\circ\text{C}$), there is very little nucleation and the formed embryos tend to grow rapidly. In this case, coarse-grained phaneritic textured rocks are formed (deep plutonic conditions). At moderate cooling rates ($\Delta T \sim 100^\circ\text{C}$), the crystal growth will be three times greater than the nucleation, but the resulting grain size will be lower than the previous case (small-grained contact facies of a cooling dyke at shallow depths). In this case, skeletal and hopper-type crystals (H-shaped) develop. They are also observed in some vitreous and aphanitic volcanic rocks. Depending on the cooling rate, if the nucleation rate is higher than the crystal growth rate, then an aphanitic texture will develop. Dendritic, skeletal, plumose and radial crystallites develop when the cooling rate is too high ($\Delta T > 100^\circ\text{C}$), as in lava flowing at the surface (Figure 11). In highly viscous felsic lavas, the atomic mobility is slow and a large ΔT can be obtained before nucleation. Watkins et al. [25] argued that once nucleation does occur, crystal growth continues, and that crystal growth rates are determined by the size of the ΔT . According to Öngen and Aysal [18], polymerization in rhyolitic magma with a high viscosity slows down diffusion and prevents nucleation, resulting in obsidian. With the undercooling (high ΔT), the usual crystal shape is inhibited and the crystals then spread from a center to form spherulites. Indeed, spherulites indicate that diffusion is the main control parameter during crystal growth. In crystal growth, matter cannot spread freely in all directions; however, each crystal develops rapidly in the fastest growth direction [18]. According to Pooja et al. [27], high undercooling promotes rapid crystallization, but it is also associated with lower magmatic temperatures and slower elemental diffusivities. Additionally, they emphasized that for crystals growing from a melt or glass of a different composition, the crystal growth rates are limited by the ability of the melt components to diffuse towards or away from the crystallization front. Moreover, they suggested that certain major and trace elements are rejected by the crystallizing phases and are concentrated at the spherulite–glass interface. The diffusion rate in silicate melts and glasses depends on the ion radius and electric charge. Large ions (such as K^+) move slowly in anhydrous glasses. In gas-saturated sections, the diffusion rate may increase locally. This facilitates both material retrieval and crystal growth [18].

In high-viscosity rhyolitic magma, the gas phase cannot be fully liberated and it collects in large bubbles. The saturated lava nature also proves that the crystallization is diffusion-controlled. After the main perlitic glass has solidified, late melts with a high internal pressure and that are saturated with water-gas (5–7%) are also collected in large bubbles [18,29]. In this case, the nucleation is reduced. As the material migration through the axiolitic channels in the fluid phase accelerates, the growth rate also increases extraordinarily. In an environment where the corners and edges of a crystal are more developed than the crystal surfaces, long sanidine cones (with a plumose structure inside) develop and then SiO_2 polymorphs such as quartz, tridymite, and cristobalite minerals settle in between [18].

Another geological material that is the subject of this study, namely, ancient metallurgical slags, is an interesting material for describing the formation processes of crystal forms similar to those in spherulites. It was determined by microscopy studies that several different crystal forms developed together in the slag samples taken from the ancient copper mine of Dereköy. As with spherulites, one of the most important parameters in the crystallization processes in slags is the undercooling processes. When the mineralogical composition of the slags was taken into account, undercooling processes were best observed in the olivine, pyroxene and magnetite minerals. A series of experimental studies have been conducted by Faure et al. (2003) on the development of olivine morphology as a function of the cooling rate and degree of undercooling [5]. They observed the evolution of the forsterite morphology, in sections parallel to the (010) plane, from tablets to hopper (skeletal) crystals, and then to swallowtail shapes (dendritic morphology) for an increased degree of undercooling. Additionally, they argued that the other shapes of olivine described

in the literature can be interpreted as particular sections of those three shapes [5]. They emphasized that the onset of dendritic growth is due to competition between the growth of the faces of the first chamber crystal and dendrite overgrowths. Experimental studies [5] have shown that regardless of the degree of undercooling (up to 116 °C), only polyhedral crystals are always produced at a low cooling rate (2 °C/h). As the cooling rate increases to 47 °C/h, the polyhedral crystals gradually disappear and most of the crystals will develop as tabular or hopper morphologies. When the undercooling changes between 60–90 °C, excessive growth of the hopper crystals develops depending on the cooling rate and baby swallowtail shaped crystals are formed. As a function of the cooling rate, only swallowtail crystals (dendrites) are formed at higher supercooling values ($-\Delta T > 70\text{--}90$ °C) [5]. The formation mechanisms of the hopper and dendritic crystals (Figures 5d–i, 7a–e and 8e–g) that we have seen in the slag samples are also compatible with the olivine experimental results and directly reflect the undercooling processes. Similar crystallization processes are also observed in suddenly-cooled basalt lavas (such as pillow lavas) [12]. Dendritic crystal formations are common in olivine, pyroxene and plagioclase minerals in basalt lavas [12]. Arzilli et al. [31] observed dendritic growth of pyroxene on initially-euhedral cores, and a surprisingly rapid increase in the crystal fraction and aspect ratio at undercooling ≥ 30 °C [30]. Another dendritic crystal form in slags is seen in magnetite minerals due to undercooling (Figures 5j–l, 7j,k and 8h–l).

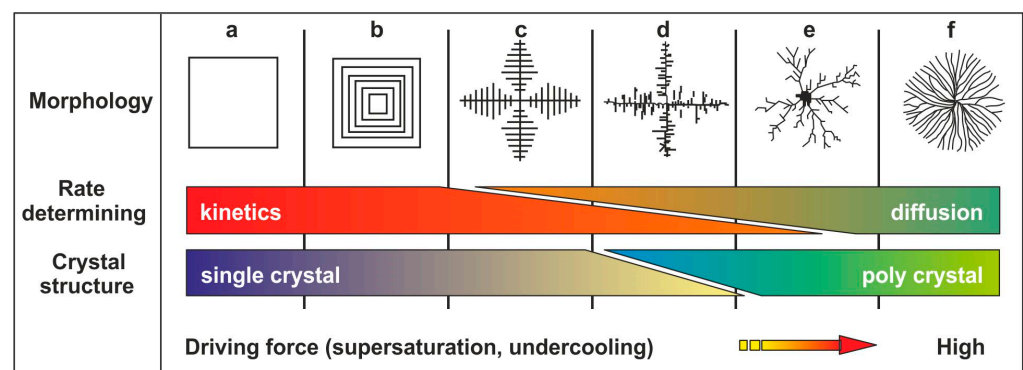


Figure 11. Schematic model showing the processes of morphological evolution: (a) polyhedral, (b) skeletal (c) single-crystalline ordered dendrite, (d) partially disordered dendrite, (e) disordered polycrystalline dendrite, and (f) dense branching morphology (taken and adopted from Meldrum and Cölfen [30]).

4.2. Crystal Morphologies

Understanding the morphology of crystals provides important information in describing the physicochemical conditions that control the formation processes of geological, biological and synthetic materials. In experimental studies [5,19], it has been determined that the cooling rate and undercooling degrees are different parameters that control nucleation and crystal growth in the later stages [5,11,12]. In a heat-controlled cooling system, euhedral crystals are observed. In undercooling conditions where the temperature control is disabled, a crystal formation sequence is observed that changes into a diffusion-controlled skeletal > baby swallowtail > swallowtail > dendrite. If diffusion is also disabled (with the radiated heat being controlled), very rapid needle-like crystallization develops in the direction of growth with heat loss [5,18,19]. Meldrum and Cölfen [30] schematically demonstrated, in their studies on the control of mineral morphologies and structures in biological and synthetic systems, the effect of gel density on the resulting crystal morphologies of the respective supersaturation (Figure 11). They suggested that, as in the melts that produce spherulites and slags, the condensation of the gel matrix reduces the diffusion rate, creating a diffusion field that destabilizes the growing surfaces, thereby developing irregularly branched polycrystalline aggregates. Moreover, theoretical studies have also shown that a decrease in diffusivity changes the morphology of the diffusion-limited aggregate from an

anisotropic shape to an irregular branching pattern [30]. Thus, the control of ion diffusion creates a morphological order of change from polyhedral to dendritic forms in descending order. Similar textural and morphological evolutionary processes were quite evident both in the feldspar minerals that made up the spherulites and in the olivine and pyroxenes in the slags.

5. Conclusions

Two different geological materials (spherulites and slags) formed by rapid cooling were primarily characterized by advanced optical and spectroscopic methods. The mineralogical and textural properties determined optically and spectroscopically were supported by mineral chemistry data obtained by SEM-EDX. Moreover, the mineralogical and micro textural features were mapped and made more visible using Raman and SEM-EDX data.

In the optical and spectroscopic characterization of the spherulite, it was determined that the main mineral phase was Na-sanidine and cristobalite, while pyrite, barite, rutile and magnetite were found in the secondary mineral phase. It was also determined that this reflects different types of crystallization processes (i.e., axiolitic, bow-tie, plumose, and spherulitic) depending on the cooling rate. Spherulites, formerly bubble fields, were composed of Na-sanidine and cristobalite crystals radiating outward from their cryptocrystalline centers. This assemblage developed mostly as a result of the devitrification of perlite glass after initial cooling induced by hydration, an interaction with groundwater, and a high temperature.

The optical and spectroscopic characterizations have shown that the slags had a wider mineralogical content. It was determined that the main mineral phase of the slags was olivine (fayalite–kirschsteinite–monticellite solid-solution) and pyroxene (hedenbergite–diopside) minerals, while minerals such as wollastonite, magnetite, and chalcopyrite were in the secondary mineral phase. The main reason for the sudden cooling textures of the slags, in which different crystal morphologies were defined (i.e., skeletal, hopper, and dendritic) depending on the cooling rate, is the collapse of the furnaces at the end of the metal melting process and the direct exposure of the gangue phase to atmospheric conditions.

Author Contributions: Conceptualization, N.A., Y.K., D.L. and M.Y.; methodology, all authors; data curation, N.A., Y.K., H.Ö., S.Ö., M.Y., G.O.I., R.F. and T.N.; writing—original draft preparation, N.A., Y.K., M.Y., S.Ö. and D.L.; writing—review and editing, all authors; visualization, N.A., M.Y., G.O.I. and R.F.; project administration, N.A.; funding acquisition, N.A., Y.K. and H.Ö. All authors have read and agreed to the published version of the manuscript.

Funding: This work was supported by the Scientific Research Projects Coordination Unit of Istanbul University-Cerrahpaşa (project nos. FDK-2017-27009 and T026/13092005).

Data Availability Statement: Not applicable.

Acknowledgments: The authors thank Onur Şimşek, Mesut İş, Gözlem Yaşayan and Ersin Kaygısız (Fatih Sultan Mehmet Vakıf University—KURAM) for their assistance in obtaining the FTIR data. R.F. and T.N. thank the Coimbra Chemistry Centre—Institute of Molecular Sciences and “Fundação para a Ciência e a Tecnologia” (Projects UIDB/00313/2020 and UIDP/00313/2020).

Conflicts of Interest: The authors declare no conflict of interest.

References

1. Keith, H.D.; Padden, F.J. The Optical Behavior of Spherulites in Crystalline Polymers. Part II. The Growth and Structure of the Spherulites. *J. Polym. Sci.* **1959**, *XXXIX*, 123–138. [[CrossRef](#)]
2. Kirov, G.N.; Ivanov, I. Crystal morphology of fayalite from copper converter slags. *Krist. Und Tech.* **1968**, *3*, 637–642. [[CrossRef](#)]
3. Nesbitt, R.V. Skeletal crystal forms in the ultramafic rocks of the Yilgarn block, western Australia: Evidence for an Archaean ultramafic liquid. *Spec. Publs Geol. Soc. Aust.* **1971**, *3*, 331–347.
4. Goldenfeld, N. Theory of spherulitic crystallization. *J. Cryst. Growth* **1987**, *84*, 601–608. [[CrossRef](#)]
5. Faure, F.; Trolliard, G.; Nicollet, C.; Montel, J.-M. A developmental model of olivine morphology as a function of the cooling rate and the degree of undercooling. *Contrib. Miner. Pet.* **2003**, *145*, 251–263. [[CrossRef](#)]

6. Faure, F.; Arndt, N.; Libourel, G. Formation of Spinifex Texture in Komatiites: An Experimental Study. *J. Pet.* **2006**, *45*, 1591–1610. [[CrossRef](#)]
7. Ichiyama, Y.; Ishiwatari, A.; Koizumi, K.; Ishida, Y.; Machi, S. Olivine-spinifex basalt from the Tamba Belt, southwest Japan: Evidence for Fe- and high field strength element-rich ultramafic volcanism in Permian Ocean. *Isl. Arc* **2007**, *16*, 493–503. [[CrossRef](#)]
8. Arndt, N.T.; Leshner, C.M.; Barns, S.J. *Komatiite*, 1st ed.; Cambridge University Press: Cambridge, UK, 2008; pp. 1–488.
9. Bouquain, S.; Arndt, N.T.; Hellebrand, E.; Faure, F. Crystallochemistry and origin of pyroxenes in komatiites. *Contrib. Miner. Pet.* **2009**, *158*, 599–617. [[CrossRef](#)]
10. Longfellow, K.M.; Swanson, S.E. Skeletal tourmaline, undercooling, and crystallization history of the Stone Mountain granite, Georgia, USA. *Can. Mineral.* **2011**, *49*, 341–357. [[CrossRef](#)]
11. Shea, T.; Houghton, B.F.; Gurioli, L.; Cashman, K.V.; Hammer, J.E.; Hobden, B.J. Textural studies of vesicles in volcanic rocks: An integrated methodology. *J. Volcanol. Geotherm. Res.* **2010**, *190*, 271–289. [[CrossRef](#)]
12. Welsch, B.; Faure, F.; Famin, V.; Baronnet, A.; Bachelery, P. Dendritic Crystallization: A Single Process for all the Textures of Olivine in Basalts? *J. Petrol.* **2013**, *54*, 539–574. [[CrossRef](#)]
13. Ding, C.; Lv, X.; Chen, Y.; Bai, C. Crystallization Kinetics of $2\text{CaO}\cdot\text{Fe}_2\text{O}_3$ and $\text{CaO}\cdot\text{Fe}_2\text{O}_3$ in the $\text{CaO}\text{--}\text{Fe}_2\text{O}_3$ System. *ISIJ Int.* **2016**, *56*, 1157–1163. [[CrossRef](#)]
14. Shea, T.; Hammer, J.E. Kinetics of cooling- and decompression-induced crystallization in hydrous mafic-intermediate magmas. *J. Volcanol. Geotherm. Res.* **2013**, *260*, 127–145. [[CrossRef](#)]
15. Aysal, N. Petrology of the Mesozoic-Tertiary Magmatism and Metamorphism in Northern Biga (Çanakale). Ph.D. Thesis, Istanbul University, Istanbul, Turkey, 2005.
16. Kurt, Y. Geological and Archaeometallurgical Investigation of the Dereköy Antique Copper Mine and Demirköy Antique Iron Mine in Strandja. Ph.D. Thesis, Istanbul University, Istanbul, Turkey, 2020.
17. Lafuente, B.; Downs, R.T.; Yang, H.; Stone, N. The power of databases: The RRUFF project. In *Highlights in Mineralogical Crystallography*; Armbruster, T., Danisi, R.M., Eds.; W. De Gruyter: Berlin, Germany, 2015; pp. 1–30.
18. Öngen, S.; Aysal, N. Kinetics of spherulitic crystallization. *Istanbul Earth Sci. Rev.* **2004**, *17*, 27–34. (In Turkish)
19. Lofgren, G. An experimental study of plagioclase crystal morphology; isothermal crystallization. *Am. J. Sci.* **1974**, *274*, 243–273. [[CrossRef](#)]
20. Brandeis, G.; Jaupart, C.; Allègre, C.J. Nucleation, crystal growth and the thermal regime of cooling magmas. *J. Geophys. Res. Solid Earth* **1984**, *89*, 10161–10177. [[CrossRef](#)]
21. Lofgren, G. Experimentally Produced Devitrification Textures in Natural Rhyolitic Glass. *GSA Bull.* **1971**, *82*, 111–174. [[CrossRef](#)]
22. Swanson, S.E.; Naney, M.T.; Westrich, H.R.; Eichelberger, J.C. Crystallization history of Obsidian Dome, Inyo Domes, California. *Bull. Volcanol.* **1989**, *51*, 161–176. [[CrossRef](#)]
23. Gránásky, L.; Pusztai, T.; Tegze, G.; Warren, J.A.; Douglas, J.F. Growth and form of spherulites. *Phys. Rev. E* **2005**, *72*, 011605. [[CrossRef](#)]
24. Castro, J.M.; Beck, P.; Tuffen, H.; Nichols, A.R.; Dingwell, D.B.; Martin, M.C. Timescales of spherulite crystallization in obsidian inferred from water concentration profiles. *Am. Mineral.* **2008**, *93*, 1816–1822. [[CrossRef](#)]
25. Watkins, J.; Manga, M.; Huber, C.; Martin, M. Diffusion-controlled spherulite growth in obsidian inferred from H_2O concentration profiles. *Contrib. Mineral. Petrol.* **2009**, *157*, 163–172. [[CrossRef](#)]
26. Rosseeva, E.; Simon, P.; Knier, R. Crystal Branching and Spherulite Formation: Similar Shapes. Different Mechanisms. *Sci. Rep. Max-Planck-Inst. Chem. Phys. Solids* **2009**, 181–185.
27. Pooja, V.K.; Hetu, C.S.; Sheila, J.S.; Badrealam, S.; Poonam, M.; Trupti, G.; Dornadula, C. Spherulites and thundereggs from pitchstones of the Deccan Traps: Geology, petrochemistry, and emplacement environments. *Bull. Volcanol.* **2012**, *74*, 559–577.
28. Lofgren, G. Experimental studies on the dynamic crystallization of silicate melts. In *Physics of Magmatic Processes*; Hargraves, R.B., Ed.; Princeton University: Princeton, NJ, USA, 1980; pp. 487–551.
29. Robert, K.S.; Robin, L.T.; Gary, E.L. Growth of megaspherulites in a rhyolitic vitrophyre. *Am. Mineral.* **2001**, *86*, 589–600.
30. Meldrum, C.F.; Helmut, C. Controlling Mineral Morphologies and Structures in Biological and Synthetic Systems. *Chem. Rev.* **2008**, *108*, 4332–4432. [[CrossRef](#)] [[PubMed](#)]
31. Arzilli, F.; Polacci, M.; La Spina, G.; Le Gall, N.; Llewellyn, E.; Brooker, R.A.; Torres-Orozco, R.; Di Genova, D.; Neave, D.A.; Hartley, M.; et al. Dendritic crystallization in hydrous basaltic magmas controls magma mobility within the Earth's crust. *Nat. Commun.* **2022**, *13*, 3354. [[CrossRef](#)]

Disclaimer/Publisher's Note: The statements, opinions and data contained in all publications are solely those of the individual author(s) and contributor(s) and not of MDPI and/or the editor(s). MDPI and/or the editor(s) disclaim responsibility for any injury to people or property resulting from any ideas, methods, instructions or products referred to in the content.